Title

General Seismic Architecture of the Southern San Andreas Fault Zone around the Thousand Palms Oasis from a Large-N Nodal Array

Journal

The Seismic Record, 2(1)

ISSN

2694-4006

Authors

Share, Pieter-Ewald
Qiu, Hongrui
Vernon, Frank L
et al.

Publication Date

2022

DOI

10.1785/0320210040

Peer reviewed

General seismic architecture of the Southern San Andreas fault zone around the Thousand Palms Oasis from a Large-N nodal array

Pieter-Ewald Share[1], Hongrui Qiu[2], Frank L. Vernon[3], Amir A. Allam[4], Yuri Fialko[3] and Yehuda Ben-Zion[5]

[1]College or Earth, Ocean, and Atmospheric Sciences, Oregon State University, Corvallis, OR

[2]Department of Earth, Atmospheric and Planetary Sciences, Massachusetts Institute of Technology, Cambridge, MA

[3]Institute of Geophysics and Planetary Physics, University of California San Diego, La Jolla, CA

[4]Department of Geology and Geophysics, University of Utah, Salt Lake City, UT

[5]Department of Earth Sciences and Southern California Earthquake Center, University of Southern California, Los Angeles, CA

Corresponding author: Pieter-Ewald Share (pieter.share@oregonstate.edu)

The Seismic Record 2022, in review

Summary

We discuss general structural features of the Banning and Mission Creek strands (BF and MCF) of the southern San Andreas fault (SSAF) in the Coachella Valley, based on ambient noise and earthquake wavefields recorded by a seismic array with >300 nodes. Earthquake P arrivals show rapid changes in waveform characteristics over 20-40 m zones that coincide with the surface BF and MCF. These variations indicate that the BF and MCF are high impedance contrast interfaces, an observation supported by the presence of seismic reflections. Another prominent but more diffuse change in SSAF structure is found ~1 km NE of the BF. This feature has average to low arrival times (P and S) and ambient noise levels (at <30 Hz), and likely represents a relatively fast velocity block sandwiched between broader MCF and BF zones. Maximal arrival delays (P~0.1 s and S~0.25 s) and highest ambient noise levels (>2 times median) are consistently observed SW of the BF, a combined effect of Coachella Valley sediments and rock damage on that side. Immediately NE of the MCF, large S minus P delays suggest a broad high V_P/V_S zone associated with asymmetric rock damage across the SSAF. This general overview shows the BF and MCF as mature but distinctly different fault zones. Future analyses will further clarify these and other SSAF features in greater detail.

1. Introduction

The Southern San Andreas Fault (SSAF) is estimated to pose one of the largest seismic risks in California (e.g., Weldon et al. 2005; Field et al. 2017). Clarifying the structural architecture and seismic properties of this major fault (Catchings et al. 2009; Lindsey & Fialko 2013; Ajala et al. 2019) can improve the estimates of potential magnitudes and shaking of future large earthquakes. Several key structural characteristics of the SSAF in the Coachella Valley remain unclear. These include the fault dip at depth (e.g., Fialko 2006; Fuis et al. 2017; Nicholson et al. 2017), the distribution of fault-related damage and slip on different fault strands (Fumal et al. 2002; Blisniuk et al. 2021), and

characteristics of velocity contrast interfaces in the fault zone (Qiu et al. 2019). To address these issues and better constrain SSAF structures, we analyze the seismic wavefield from local earthquakes (Fig. 1a) recorded across a large-N array spanning a northern multi-stranded section of the SSAF near the Thousand Palms Oasis Preserve in the Coachella Valley (Fig. 1b). To compensate for the relative paucity of seismicity in the area, we also analyze data from regional and teleseismic earthquakes (Fig. 1a inset) and ambient seismic noise.

The >300 node array transected both the Banning (BF) and Mission Creek (MCF) fault strands of the SSAF near the Thousand Palms Oasis, California, about 10 km northwest of Biskra Palms (e.g., Behr et al. 2010) where these two strands merge (Fig. 1a). Near the surface, the BF and MCF together with other minor faults comprise a >2 km wide fault zone embedded in Pliocene and Pleistocene stratified rocks, with thick Quaternary Coachella Valley sediments to the SW and thinner sediments immediately NE of the MCF (Rymer 2000). Cretaceous plutonic rocks of the Peninsular Ranges underlie the Valley sediments (e.g., Matti et al. 1992; Ajala et al. 2019), whereas older metamorphic and igneous intrusive rocks of the Little San Bernardino Mountains likely abut the MCF beneath shallow sediments to the NE (Catchings et al. 2009). Around the study site little is known about internal features of the SSAF structure, including the width and depth of core and broader damage zones, deeper attitudes of the BF and MCF, seismic velocity (V_P and V_S) contrasts and variations across the fault zone, and evidence for crustal fluids. There is evidence for a steep NE dipping electrically conductive SSAF fault zone in the upper crust (~3 km wide at the surface) from electromagnetic imaging (Share et al. 2022). Active source seismic exploration and potential field results indicate similar near-surface geometries for the surrounding SSAF (e.g., Fuis et al. 2017). To understand these and other features better, we apply a range of tools well-suited for imaging internal fault zone features (e.g, Ben-Zion et al. 2015; Share et al. 2019a; Qin et al. 2020; Qiu et al. 2021). In the present paper we focus on general aspects of the recorded data such as the arrival time, frequency, amplitude and phase variations across

the array from direct, reflected and transmitted seismic phases.

2. Data

The nodal array (Fig. 1) was deployed in the beginning of March 2020 and consisted of 322 Zland 3-component 5 Hz nodes recording at 500 samples per second (Vernon et al. 2020). Most of these nodes recorded into early April. The array configuration included two 100+ node 2-D subarrays with apertures of 0.6-1 km centered on the BF and MCF (Fig. 1b). Each subarray included a grid of regularly spaced nodes, as well as several nodes scattered around that grid. In addition, we deployed a ~4 km-long 100+ node quasi-linear profile crossing both strands and connecting the two subarrays (Fig. 1b). The inter-node spacing varied from ~15 m around fault traces to ~100 m away from them. Four nodes were installed farther NE (Fig. 1a) to help constrain local seismicity in the region but data from these nodes were not analyzed in this general study.

During acquisition, the array recorded several local earthquakes of which we analyzed high quality data from 27 M>1 events that had diverse hypocentral distances (<100 km) and azimuths relative to the array (Fig. 1a & Table S1). In addition, we analyzed data from 5 moderate to large regional earthquakes (<30° away), including the M 5.7 Magna (Utah) and M 6.5 Stanley (Idaho) events, and 3 teleseismic events (>30° away) (Fig. 1a inset & Table S2). Earthquake metadata were obtained from the Southern California Earthquake Data Center (SCEDC, 2013). Three-component waveforms associated with these events were extracted from the continuous recordings and detrended. In addition, a 2-20 Hz bandpass filter was applied to the local waveforms and a 1 Hz lowpass filter was applied to the teleseismic and regional waveforms. The lower frequency data provide information about large-scale variations across the linear profile and the higher frequency waveforms give insight into smaller-scale complexities along this profile and across the two dense subarrays. The entire continuous dataset was used during ambient noise analysis.

3. Analysis and Results

To obtain a general sense of large-scale structural changes across the linear profile we analyzed early waveform similarities and delay times of teleseismic and regional P arrivals. For a given event the first P maxima/minima coherent across vertical component recordings were picked and designated P arrivals (Fig. 2a). Each 3 s early P waveform (0.5 s before and 2.5 s after P pick) was then cross-correlated with every other 3 s P waveform in the linear array and the maximum correlation coefficients were cataloged. The delays corresponding to the maximum correlation coefficients across the array are consistent with the delays obtained through manual picking. High correlation coefficients between neighboring stations imply similar large-scale structure beneath those stations. Low coefficients pinpoint a transition between two dissimilar media (e.g., Qin et al. 2021).

Cross-correlation results for three representative events are shown in Fig. 2b. Given different azimuths and inclination angles of the incoming wavefronts, the cross-correlations exhibit some variability between events. Nevertheless, taken together, Fig. 2 suggests three locations of large-scale structural changes. One of these occurs over a 20-40 m wide zone near a mapped central strand of the BF (station 21 in Fig. 1b) and another around the MCF proper over a similarly narrow zone. A third region of rapid waveform changes is associated with a yet unknown structure around station 60 (Figs 1b & 2). We therefore classify the site in terms of four crustal zones, one SW of the BF, a second from the mapped BF to about ~1 km in the NE, a third from that point to the mapped MCF and the final zone extending from the MCF northeastwards.

Next, we inspected the delay time results from all teleseismic and regional events to help quantify the general P wave velocity (V_P) variations across the profile. For each event, the picked arrival times were corrected for array geometry by subtracting the predicted travel times to individual stations using the TauP algorithm (Crotwell et al. 1999) and the IASP91 global velocity model (e.g., Share et al. 2019a; Qin et al. 2021; Qiu et al. 2021). A correction was then made for elevation above sea level by subtracting the excess travel times to elevated stations calculated with a reference near-surface V_P=2 km/s (from Ajala et al. 2019). In this study, the choice of reference V_P has a minor effect

on delay time estimates as the change in elevation from station 1 to 151 is only 138 m (Vernon et al. 2020), which is a small fraction of the ~4 km profile length and probably below the length-scale resolution of the several kilometer wavelengths of the teleseismic/regional waves. Finally, for each event the median delay of the array was subtracted from individual station delays to provide a relative measure of delay/slowness across the array. After corrections, the median of all event delay times shows a clear trend of increasing slowness (decreasing V_P) from NE to SW (Fig. 3a). This likely reflects a large-scale change in upper crustal structure from crystalline bedrock in the NE (high V_P, Catchings et al. 2009) to thick Coachella Valley sediments in the SW (low V_P, Ajala et al. 2019) (Fig. 3a).

To provide information on smaller-scale complexities, we analyzed the higher frequency information provided by local earthquake arrivals. For the 27 high quality events, we picked P arrivals manually for linear array stations on vertical component recordings (Fig. 3b). For the 14 clear S arrival producing events, we picked S arrivals on both horizontal components and took the average of the two picks to produce a single S pick per event and per station (Fig. 3b). These picks were corrected for their respective propagation paths using the 3D V_P and V_S models of Share et al. (2019b). Again, for each event and each phase, the median delay was subtracted from individual station delays to provide a relative measure of P and S delays across the array. The resultant median P and S delay times for all events (Fig. 3a) reflect upper crustal features not captured by the regional 3D velocity models, i.e., internal features of the SSAF structure at the site.

In addition to a general increase in delay (slowness) as shown by the teleseismic/regional earthquake results, the local delay time curves reveal two other key characteristics; peak P and S delays (~0.1 s and ~0.25 s) within a 200 m zone SW of the BF and, relative to P, rapidly increasing S delays within a >500 m zone around the BF and immediately NE of the MCF within a similarly sized zone. These are relatively high V_P/V_S regions as the S arrivals are disproportionately delayed compared to P. The cause of high V_P/V_S SW of BF is likely a combination of thick sediments (usually $V_P/V_S>>2$, Brocher 2005), rock damage around that fault and associated fluids. Sediments cannot be

the only cause as they gradually increase in thickness (Fig. 3a) up to ~2 km in the central Coachella Valley (west of the study site, Ajala et al. 2019) but the observed P, S and S minus P delays peak around the BF. This suggests rock damage along the BF is a contributing factor. There is significantly less and decreasing sediment coverage NE of the MCF, and we associate most of the high V_P/V_S there to asymmetric rock damage on that side, which is potentially infiltrated by the same fluids feeding the nearby oases. The asymmetric nature of brittle damage is supported by the presence of several mapped minor faults NE of the MCF and none immediately to the SW (Fig. 1b). Assuming this high V_P/V_S structure extends to a depth of 4 km implies a V_P/V_S>2.15, which is the average V_P/V_S in the uppermost 4 km of the local crust in the Share et al. (2019b) models. A depth of 4 km is approximately the extent of damage-related high electrical conductivities in the area (Share et al. 2022) and fault zone damage along other major faults (e.g., Qin et al. 2021; Qiu et al. 2021).

Local earthquake full waveforms provide additional information on fault zone characteristics (Fig. 3b). The region around station 60 acts as an inflection point where incoming wavefronts undergo a sudden change in azimuth and/or apparent slowness. The Supplementary Material illustrates similar rapid changes in three-component motion around station 60 for an example teleseismic event (Movie S1). Also, P and S reflected phases emanate from the BF and MCF but not the region around station 60. These show the BF and MCF are sharp high impedance contrast interfaces whereas the region around station 60 likely represents a more diffuse change in structure.

Finally, we quantified variations in the background ambient noise levels across the array at different frequencies, which provides a multi-scale measure of near-surface ground amplification and attenuation properties. In addition to the typical low frequency ambient noise from remote natural sources (e.g., ocean waves), there are strong local sources producing noise at frequencies >1 Hz. These include primarily frequent daily road and rail traffic in the Coachella Valley (Brenguier et al. 2019), and traffic along the Thousand Palms Canyon Road (Fig. 1b). The latter is near-parallel to the linear profile along most of its length and is offset to the northwest by ~200 m, providing a relatively

uniform source of noise to the entire array. For each of the frequency ranges <5 Hz, 5-10 Hz, 10-15 Hz, 15-20 Hz, 20-25 Hz and 25-30 Hz, we applied a bandpass filter to each 24-hour recording for each station and calculated the median of the respective energy envelopes. This was done separately for the vertical and each horizontal component recording after the latter were rotated by 38° E of N to align with mean fault-normal and fault-parallel coordinates.

Over a wide frequency range, the ambient noise results corroborate a change from relatively stiff (crystalline bedrock) in the NE to relatively compliant (thick unconsolidated Coachella Valley sediments) in the SW, with a rapid increase in noise level towards the SW around BF with the Valley sediments producing the maximum noise level (>2 times the medial level, Fig. 4a). The effects of near-surface structures on ambient noise recordings are clearly greater than the proximity to local high-frequency noise sources as, for example, the Thousand Palms Canyon Road is closest to the intersection of the linear profile and the MCF (Fig. 1b) but the region SW of the BF consistently experiences the highest noise levels (Fig. 4a). At frequencies lower than 15 Hz, there are some elevated noise levels in a ~100 m zone immediately NE of the MCF (Fig. 4b & Movie S2), potentially the surface manifestation of a core damage structure within the broader asymmetric damage zone (e.g., Fig. 3a). Higher median absolute deviations (MAD) of the noise field around the BF (Fig. 4a) point to greater time-dependent near-surface structural changes in response to atmospheric and other sources (e.g., rainfall, air pressure, etc.) (Movies S3-S4). Moreover, the 5-10 Hz band shows rapid variations in fault-parallel minus fault-normal ground motions within this zone and especially around station 21 (Fig. 4b & Movie S5). This suggests the broader BF zone has anisotropic properties. Finally, the region around station 60 has associated average to minimal ambient noise levels (Fig. 4), highlighting a lack of unconsolidated sediments and/or damage-related materials in this zone of diffuse structural change.

4. Discussion and Conclusions

At large-scale, seismic velocities generally decrease from NE to SW as near-surface crystalline bedrock (low ambient noise levels) transitions to unconsolidated Coachella Valley sediments (highest ambient noise levels) (Figs 3 & 4, Movies S3-S4). This general change is not smooth and includes abrupt changes in structure near a central strand of the BF strand (station 21), the MCF proper (station 98) and in a region around station 60 (Figs 2 & 3b, Movie S1). Also present are >500 m-wide low velocity, high V_P/V_S fault damage related structures around the BF and immediately NE of MCF (asymmetric) (Fig. 3a). The total contribution of fault damage to the elevated high V_P/V_S around the BF is unclear, but NE of the MCF it is likely the main cause. On that side of the MCF the upper crustal fractures and pores within this region of active damage production may be infiltrated by crustal fluids from various sources (e.g., Catchings et al. 2009; Share et al. 2022). The region around station 60 is characterized by average to low slowness, V_P/V_S and ambient noise levels, which we interpret as a relatively intact faster velocity block sandwiched between broader BF and MCF zones.

Overall, both the BF and MCF exhibit crustal structures characteristic of mature faults. The BF strand separates two crustal blocks of very different material properties whereas the MCF is actively deforming (e.g., Blisniuk et al. 2021) and likely has strong asymmetric damage. The latter is a signature of persistent ruptures along a bimaterial interface with greater damage generation on the competent rock side (crystalline basement in NE) of the interface (e.g., Ben-Zion & Shi 2005; Dor et al. 2008; Share et al. 2019a). For a dextral strike-slip earthquake, this bimaterial contrast polarity may induce preferred sub-shear velocity propagation in the direction of motion of the slow compliant block (Shlomai et al. 2020), i.e., towards the NW in this case (e.g., Bombay Beach M=7.8 earthquake scenario, Field et al. 2017). We note that this velocity contrast polarity is opposite to that observed at ~10 km depth along a major structure NE of the mapped SSAF (Qiu et al. 2019; Share et al. 2019b), which implies depth-dependent contrast polarities if the deeper structure is a downdip continuation of the SSAF and subsequently more complex earthquake rupture dynamics. Moreover, compared to younger faults (e.g., SJFZ), the large BF and MCF damage zone dimensions (>500 m) indicate a fault system

impacted by several large seismic (and potentially aseismic) events (Mitchell & Faulkner 2009). Additional details on the seismic structure of the SSAF in the study area can be obtained by analyzing fault zone head and trapped waves (e.g., Qin et al. 2021; Qiu et al. 2021), reverse-time migration of fault-reflected phases, and migration of the scattered wavefield (Touma et al. 2021). Analyses of such signals are the subject of continuing research.

Acknowledgements

We thank Deborah Rogers and Ginny Short (Center for Natural Lands Management) and Brian Ousley (Bureau of Land Management) for help with permitting at the Thousand Palms site. We also acknowledge the IRIS Passcal Instrument Center and the University of Utah Seismograph Stations for providing nodal seismometers. Constructive comments from the editor Dr. Keith Koper and two anonymous reviewers helped to improve the manuscript. The deployment and retrieval of nodes were made possible through the dedication and hard work of students, post docs, faculty and staff from the University of Southern California, Southern California Earthquake Center, UCSD/Scripps Institution of Oceanography, University of Utah, San Diego State University, the USGS and the NASA Jet Propulsion Laboratory. This study was supported by the National Science Foundation (grants EAR-1841315 and 1841273) and P.-E. Share was also supported by a Green Foundation Postdoctoral Fellowship (UCSD/Scripps).

Data Availability

All data are freely available for download from the IRIS DMC (Vernon et al. 2020).

Conflict of Interest

The authors declare that they have no competing interests.

Supplementary Materials

Movies S1-S5. Movie S1 is a three-component motion animation of event e2 in Fig. 2. Movies S2-S5 are time lapses over a roughly month-long window of the same data used to produce Fig. 4b (in this subfigure the medians over that month are shown). Figure S1 shows additional S-wave arrivals and picks for the local events e5 and e6 in Fig. 3b. Tables S1 and S2 contain metadata for the local and teleseismic earthquakes used during analysis.

References

Ajala, R., Persaud, P., Stock, J. M., Fuis, G. S., Hole, J. A., Goldman, M. R., & Scheirer, D. S. (2019). Three-dimensional basin and fault structure from a detailed seismic velocity model of Coachella Valley, Southern California. Journal of Geophysical Research, 124(5), 4728-4750.

Behr, W. M., Rood, D. H., Fletcher, K. E., Guzman, N., Finkel, R., Hanks, T. C., Hudnut, K. W., Kendrick, K. J., Platt, J. P., Sharp, W. D., Weldon, R. J. & Yule, J. D. (2010). Uncertainties in slip-rate estimates for the Mission Creek strand of the southern San Andreas fault at Biskra Palms Oasis, southern California. Geological Society of America Bulletin, 122, 1360-1377.

Ben-Zion, Y. and Z. Shi, 2005. Dynamic rupture on a material interface with spontaneous generation of plastic strain in the bulk, *Earth Planet. Sci. Lett.*, 236, 486-496, DOI: 10.1016/j.epsl.2005.03.025.

Ben-Zion, Y., Vernon, F. L., Ozakin, Y., Zigone, D., Ross, Z. E., Meng, H., White, M., Reyes, J., Hollis, D., & Barklage, M. (2015). Basic data features and results from a spatially dense seismic array on the San Jacinto fault zone. *Geophysical Journal International*, *202*(1), 370–380. https://doi.org/10.1093/gji/ggv142

Blisniuk, K., Scharer, K., Sharp, W. D., Burgmann, R., Amos, C., & Rymer, M. (2021). A revised position for the primary strand of the Pleistocene-Holocene San Andreas

fault in southern California. *Science Advances*, *7*(13), eaaz5691. https://doi.org/10.1126/sciadv.aaz5691

Brenguier, F., P. Boué, Y. Ben-Zion, F. Vernon, C. Johnson, A. Mordret, O. Coutant, P.-E. Share, E. Beaucé, D. Hollis and T. Lecocq, 2019. Turning Vehicle Traffic into a Powerful Seismic Source for Monitoring Active Faults, *Geophys.*, *Res. Lett.*, 46, 9529-9536, doi: 10.1029/2019GL083438.

Brocher, T. M. (2005). Empirical relations between elastic wavespeeds and density in the Earth's crust. *Bulletin of the Seismological Society of America, 95*(6), 2081-2092.

Catchings, R. D., Rymer, M. J., Goldman, M. R., & Gandhok, G. (2009). San Andreas Fault Geometry at Desert Hot Springs, California, and Its Effects on Earthquake Hazards and Groundwater. *Bulletin of the Seismological Society of America*, *99*(4), 2190–2207. https://doi.org/10.1785/0120080117

Crotwell, H. P., Owens, T. J., & Ritsema, J. (1999). The TauP Toolkit: Flexible seismic travel-time and ray-path utilities, *Seismological Research Letters*, 70(2), 154-160.

Dor, O., Yildirim, C., Rockwell, T.K., Ben-Zion, Y., Emre, O., Sisk, M., Duman, T. Y., 2008. Geologic and geomorphologic asymmetry across the rupture zones of the 1943 and 1944 earthquakes on the North Anatolian Fault: possible signals for preferred earthquake propagation direction, *Geophys. J. Int.*, 173, 483–504, doi: 10.1111/j.1365-246X.2008.03709.x.

Fialko, Y. (2006). Interseismic strain accumulation and the earthquake potential on the southern San Andreas fault system, Nature, 441, 968-971, doi:10.1038/nature04797

Field, E. H., Jordan, T. H., Page, M. T., Milner, K. R., Shaw, B. E., Dawson, T. E., … Thatcher, W. R. (2017). A Synoptic View of the Third Uniform California Earthquake Rupture Forecast (UCERF3). *Seismological Research Letters*, *88*(5), 1259–1267. https://doi.org/10.1785/0220170045

Fuis, G. S., Bauer, K., Goldman, M. R., Ryberg, T., Langenheim, V. E., Scheirer, D. S., Rymer, M. J., Stock, J. M., Hole, J. A., Catchings, R. D., Graves, R. W., & Aagaard, B. (2017). Subsurface geometry of the San Andreas Fault in Southern California: Results from the Salton Seismic Imaging Project (SSIP) and strong ground motion expectations. Bulletin of the Seismological Society of America, 107(3), 1642-1662.

Fumal, T. E., Rymer, M. J., & Seitz, G. G. (2002). Timing of Large Earthquakes since A.D. 800 on the Mission Creek Strand of the San Andreas Fault Zone at Thousand Palms Oasis, near Palm Springs, California. *Bulletin of the Seismological Society of America*, *92*(7), 2841–2860. https://doi.org/10.1785/0120000609

Lindsey, E. O., & Fialko, Y. (2013). Geodetic slip rates in the southern San Andreas Fault system: Effects of elastic heterogeneity and fault geometry. Journal of Geophysical Research, 118, 689-697.

Matti, J. C., Morton, D. M., & Cox, B. F. (1992). The San Andreas fault system in the vicinity of the central Transverse Ranges province, southern California, U.S. Geological Survey Open-File Report 92-354.

Mitchell, T. M., & Faulkner, D. R. (2009). The nature and origin of off-fault damage surrounding strike-slip fault zones with a wide range of displacements: A field study from the Atacama fault system, northern Chile. Journal of Structural Geology, 31(8), 802-816.

Nicholson, C., A. Plesch and J.H. Shaw (2017). Community Fault Model Version 5.2: Updating & expanding the CFM 3D fault set and its associated fault database, *2017 SCEC Annual Meeting Proceedings & Abstracts*, XXVII, poster 234, p.142-143.

Qin, L., Share, P.-E., Qiu, H., Allam, A. A., Vernon, F. L., & Ben-Zion, Y. (2021). Internal structure of the San Jacinto fault zone at the Ramona Reservation, north of Anza, California, from dense array seismic data. *Geophysical Journal International*, *224*(2), 1225–1241. https://doi.org/10.1093/gji/ggaa482

Qiu, H., Lin, F.-C., & Ben-Zion, Y. (2019). Eikonal tomography of the Southern California plate boundary region, Journal of Geophysical Research, 124, 9755-9779, doi: 10.1029/2019JB017806.

Qiu, H., Ben-Zion, Y., Catchings, R., Goldman, M. R., Allam, A. A., & Steidl, J. (2021). Seismic Imaging of the Mw 7.1 Ridgecrest Earthquake Rupture Zone From Data Recorded by Dense Linear Arrays. *Journal of Geophysical Research: Solid Earth*, *126*(7), e2021JB022043. https://doi.org/https://doi.org/10.1029/2021JB022043

Rymer, M. J. (2000). Triggered Surface Slips in the Coachella Valley Area Associated with the 1992 Joshua Tree and Landers, California, Earthquakes. *Bulletin of the Seismological Society of America*, *90*(4), 832–848. https://doi.org/10.1785/0119980130

SCEDC (2013). Southern California Earthquake Data Center. Caltech.Dataset. doi:10.7909/C3WD3xH1.

Share, P.-E., Allam, A. A., Ben-Zion, Y., Lin, F.-C., & Vernon, F. L. (2019a). Structural Properties of the San Jacinto Fault Zone at Blackburn Saddle from Seismic Data of a Dense Linear Array. *Pure and Applied Geophysics*, *176*(3), 1169–1191. https://doi.org/10.1007/s00024-018-1988-5

Share, P.-E., Guo, H., Thurber, C. H., Zhang, H., & Ben-Zion, Y. (2019b). Seismic Imaging of the Southern California Plate Boundary around the South-Central Transverse Ranges Using Double-Difference Tomography. *Pure and Applied Geophysics*, *176*(3), 1117–1143. https://doi.org/10.1007/s00024-018-2042-3

Share, P.-E., Peacock, J. R., Constable, S. C., & Vernon, F. L. (2022). Structural properties of the Southern San Andreas fault zone in northern Coachella Valley from magnetotelluric imaging. *Geophysical Journal International*, in review.

Shlomai, H., Kammer, D. S., Adda-Bedia, M., & Fineberg, J. (2020). The onset of the frictional motion of dissimilar materials. *Proceedings of the National Academy of Sciences*, *117*(24), 13379 LP – 13385. https://doi.org/10.1073/pnas.1916869117

Touma, R., Blondel, T., Derode, A., Campillo, M., & Aubry, A. (2021). A distortion matrix framework for high-resolution passive seismic 3-D imaging: application to the San Jacinto fault zone, California. Geophysical Journal International, 226(2), 780-794.

Vernon, F., Share, P.-E., Ben-Zion, Y., Fialko, Y., & Allam, A. (2020). Southern San Andreas Fault Zone [Data set]. International Federation of Digital Seismograph Networks. https://doi.org/10.7914/SN/YA_2020

Weldon, R. J., Fumal, T. E., Biasi, G. P., Scharer, K. M. (2005). Past and future earthquakes on the San Andreas fault, Science, 308, 966-967.

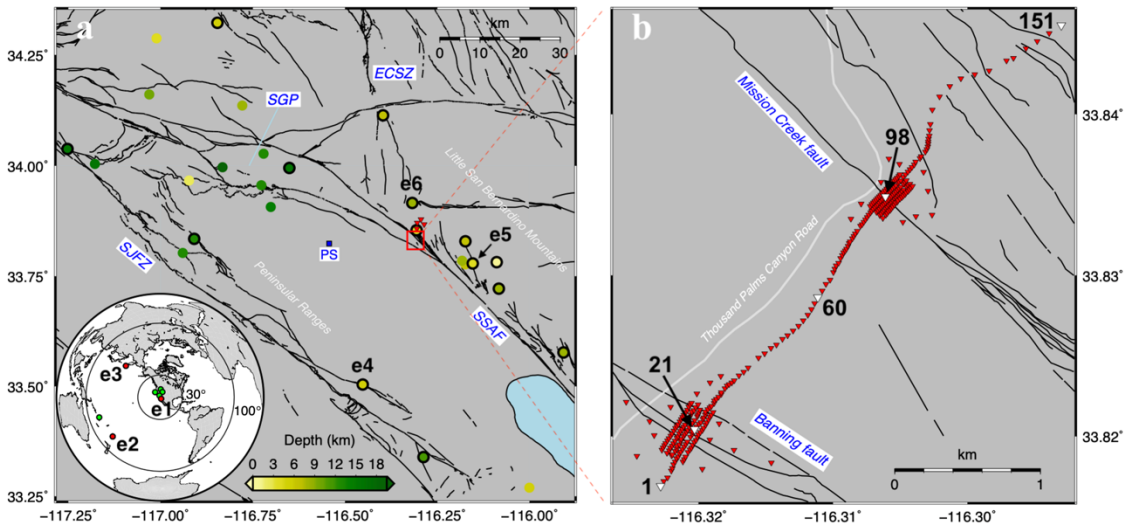

Figure 1: Study area in the context of the Southern San Andreas fault (SSAF). (a) Major fault surface traces (black lines) and local earthquakes (circles, colors indicate depth) analyzed in this

study. P waveforms from all events are analyzed whereas S waveform data from only 14 events (thick-outlined circles) are used. Example events from Figs 2-4 are labeled. The dense array is indicated (red box) along with four subsidiary stations north of the array not used in this study (red triangles). San Gorgonio Pass (SGP), the Eastern California Shear Zone (ECSZ), the San Jacinto fault zone (SJFZ) and the town of Palm Springs (PS) are shown for reference. The global map (inset) shows the eight regional (epicenters <30° away) and teleseismic (epicenters 30°-100° away) earthquakes employed in this study (circles), with example events labeled. (b) Zoom in on the red box in (a) showing the Banning (BF) and Mission Creek (MCF) faults and the nodal array (red triangles). Some nodes along the long linear profile are highlighted for reference and the nearby Thousand Palms Canyon Road is also shown.

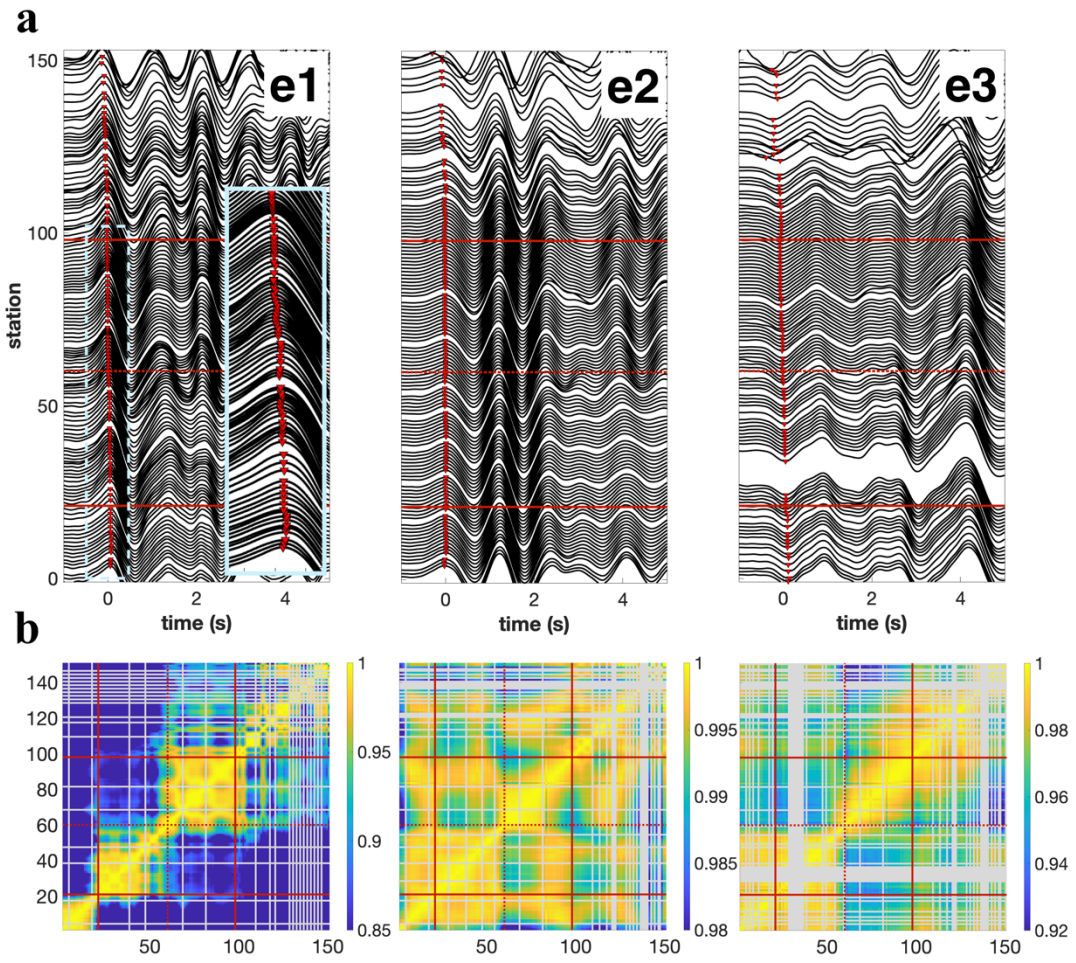

Figure 2: Teleseismic and regional earthquake analysis. (a) Vertical component P-wave recordings from three example teleseismic/regional earthquakes (e1-e3, locations in Fig. 1a inset).

The solid lines at stations 21 and 98 indicate mapped BF and MCF locations. The dashed line at station 60 highlights another region of rapid changes in waveform characteristics. The zoom in on event e1 early P waves (-0.3 s to 0.3 s) highlights the changes in delay between stations 1 to 100 for these lower frequency signals. (b) Maximum cross-correlation coefficients between early P waveforms (3 s) across the linear array for each event in (a). Note the change in color scale. Gray lines are missing stations.

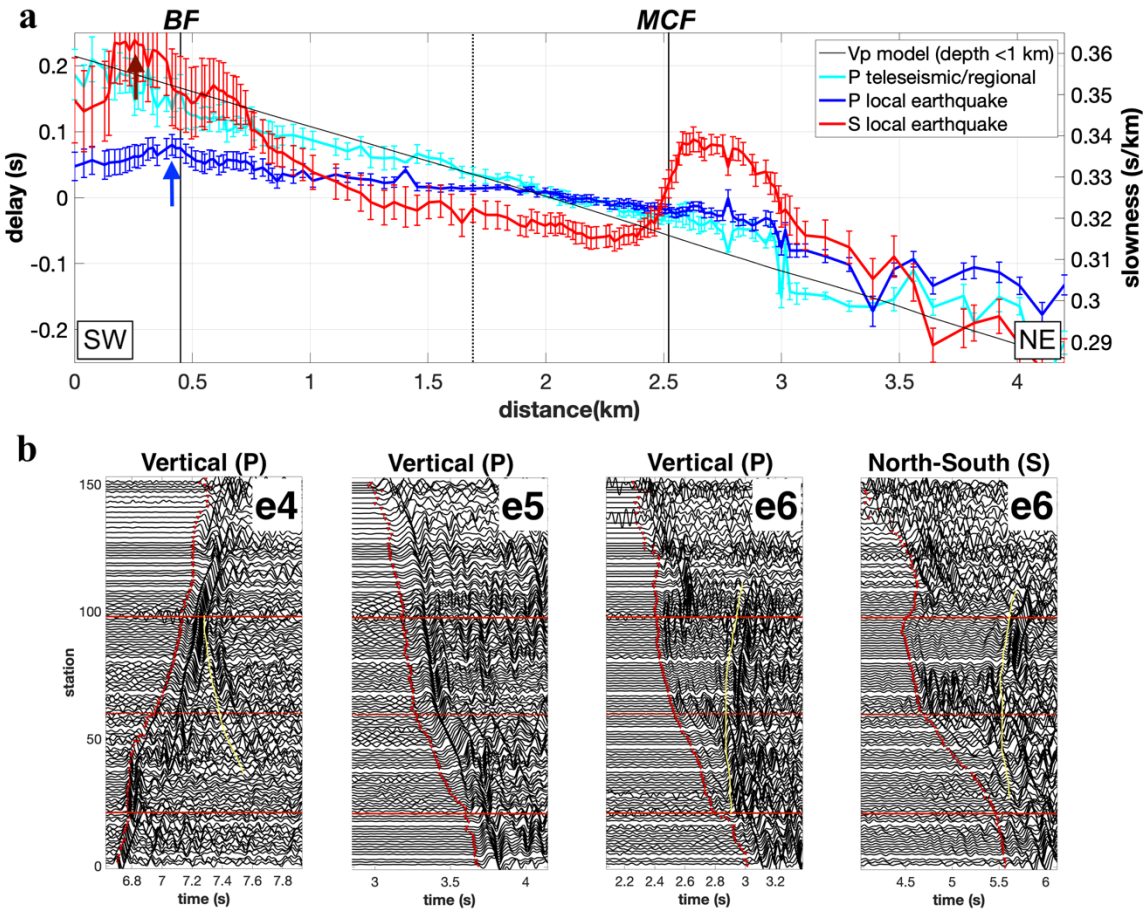

Figure 3: Delay time analysis and local earthquake waveforms. (a) Median delay time curves for all teleseismic/regional (8, cyan), local P (27, blue) and local S (14, red) arrivals. Blue and maroon arrows show the peaks in local P and S delays. The error bars equal 1 standard error converted from the median absolute deviations (MAD) for each station using $\sqrt{\pi/2}\cdot MAD/\sqrt{N}$, where N is the number of events. The black trendline indicates average slowness in the uppermost 1 km of the V_P model of Ajala et al. (2019), a proxy value for increasing sediment thickness towards the SW. Vertical black lines from left to right are the BF, station 60 and the MCF. (b) P

and S waveforms from example local earthquakes (e4-e6). First three panels are P, the last is S. Instead of a 2-20 Hz bandpass (P), a 2-10 Hz filter is applied to S for better waveform illumination. See Fig. 1a for e4-e6 locations and Fig. S1 for S waveforms and picks associated with both horizontal components for example events e5 and e6. Horizontal red lines have the same meaning as in Fig. 2. Yellow curves indicate reflections off the MCF (e4) and BF (e6).

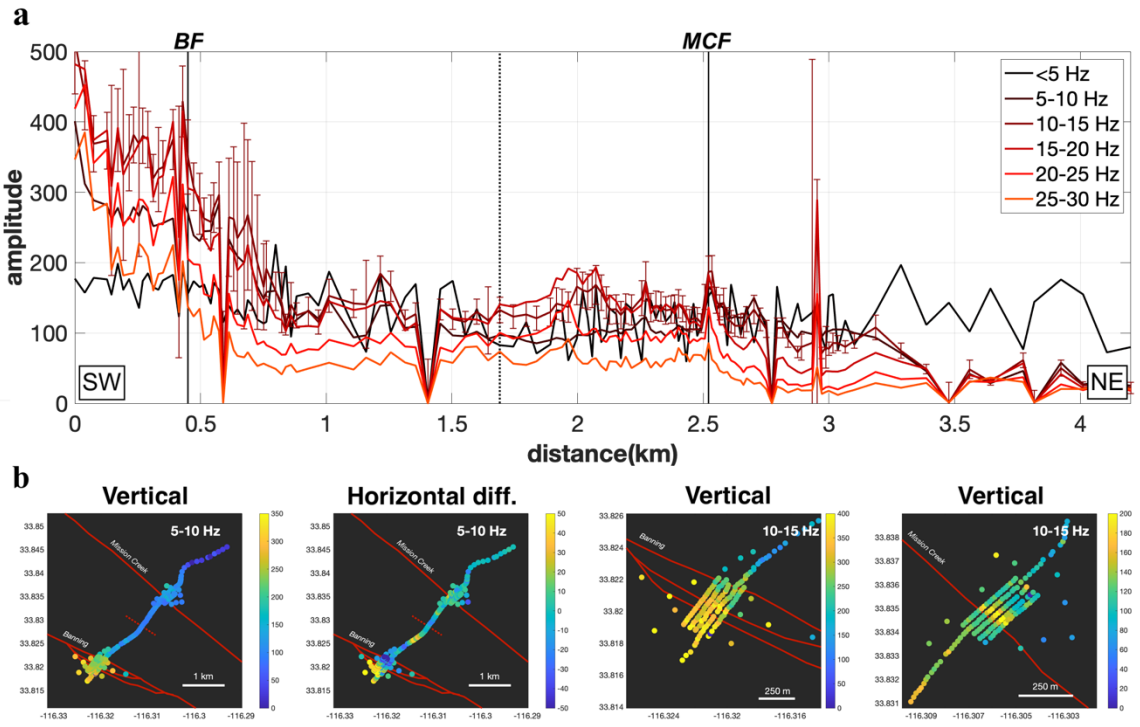

Figure 4: Ambient noise analysis. (a) Median ambient noise levels (vertical component) in different frequency bands over roughly a month-long period (recording day 63 to 90). As an example, MADs for the 10-15 Hz band are also shown. This indicates median variability across the month-long window. Vertical black lines have the same meaning as in Fig. 3a. Note the increase in MAD/variability around the BF. (b) Median ambient noise levels in map view for the same time window at 5-10 Hz for the entire array (left two panels) and at 10-15 Hz focused on the BF and MCF (right two panels). The short dashed red line in the left two panels point to the location of station 60 and a region of relatively diffuse change in structure. Note the change in color scale between panels. All panels show vertical component motions except the second, which indicates fault-parallel minus fault-normal motions. Movies associated with these are in the Supplementary Materials (Movies S2-S5).